PNAS RESEARCH ARTICLE | CHEMISTRY

Boosting the reaction kinetics in aprotic lithium-carbon dioxide batteries with unconventional phase metal nanomaterials

Jingwen Zhou[a,b,d,1], Tianshuai Wang[c,1], Lin Chen[d,1], Lingwen Liao[a,1], Yunhao Wang[a], Shibo Xi[e], Bo Chen[a], Ting Lin[f,g], Qinghua Zhang[f,g], Chenliang Ye[h], Xichen Zhou[a], Zhiqiang Guan[a], Li Zhai[a,b], Zhen He[a,b], Gang Wang[i], Juan Wang[a], Jinli Yu[a], Yangbo Ma[a], Pengyi Lu[a,b], Yuecheng Xiong[a], Shiyao Lu[a], Ye Chen[i], Bin Wang[j], Chun-Sing Lee[a,k], Jianli Cheng[d,2], Lin Gu[f,g,2], Tianshou Zhao[c,2], and Zhanxi Fan[a,b,l,2]

Edited by Jill Millstone, University of Pittsburgh, Pittsburgh, PA; received March 16, 2022; accepted August 25, 2022 by Editorial Board Member Chad A. Mirkin

Given the high energy density and eco-friendly characteristics, lithium-carbon dioxide (Li-CO_2) batteries have been considered to be a next-generation energy technology to promote carbon neutral and space exploration. However, Li-CO_2 batteries suffer from sluggish reaction kinetics, causing large overpotential and poor energy efficiency. Here, we observe enhanced reaction kinetics in aprotic Li-CO_2 batteries with unconventional phase 4H/face-centered cubic (fcc) iridium (Ir) nanostructures grown on gold template. Significantly, 4H/fcc Ir exhibits superior electrochemical performance over fcc Ir in facilitating the round-trip reaction kinetics of Li^+-mediated CO_2 reduction and evolution, achieving a low charge plateau below 3.61 V and high energy efficiency of 83.8%. Ex situ/in situ studies and theoretical calculations reveal that the boosted reaction kinetics arises from the highly reversible generation of amorphous/low-crystalline discharge products on 4H/fcc Ir via the Ir-O coupling. The demonstration of flexible Li-CO_2 pouch cells with 4H/fcc Ir suggests the feasibility of using unconventional phase nanomaterials in practical scenarios.

unconventional phase | Ir nanostructures | reaction kinetics | electrochemical mechanism | Li-CO_2 battery

Significance

High theoretical energy density and "carbon-neutral" capability enable aprotic Li-CO_2 batteries to attract rapidly increasing interests in the big picture of the sustainable development of humankind, but they suffer from sluggish reaction kinetics, causing large overpotential and poor energy efficiency. Existing strategies mainly focus on optimizing the morphology, size, composition, and distribution of cathode catalysts to boost the Li^+-mediated redox reactions. However, another critically important structural parameter, crystal phase, is barely explored. Here, unconventional phase 4H/face-centered cubic (fcc) Ir nanostructures were synthesized as the catalysts for Li-CO_2 batteries, which demonstrates much more superior electrochemical performance over common fcc Ir-based counterparts, revealing the great potential of the phase engineering of catalysts in metal-gas batteries.

Featuring high theoretical energy density (1,875 mAh g^{-1}) and environmentally friendly properties, the lithium-carbon dioxide (Li-CO_2) battery, a metal-gas electrochemical system, has been regarded in recent years as a promising candidate for next-generation high-performance energy conversion and storage techniques with carbon-neutral capability (1–3). The Li-CO_2 battery can not only act as a durable power source but also offer an efficient strategy for CO_2 fixation without extra energy consumption, which is hardly achieved by the traditional CO_2 fixation methods in industry. These favorable characteristics make Li-CO_2 batteries extremely attractive and important in terms of sustainable development and space exploration (4–6). Moreover, the deeper investigation of Li-CO_2 electrochemistry also facilitate the development of Li-O_2 batteries toward real Li-air batteries that can steadily operate in ambient atmosphere (7, 8).

At the initial stage, various carbon materials (e.g., super P (9), Ketjen black (10), carbon nanotube (11–13), graphene (14–17)) have been used as cathode catalysts in aprotic Li-CO_2 batteries to deliver large specific capacity because of their high specific surface area. Unfortunately, owing to the low catalytic activity of carbon materials, Li-CO_2 electrochemistry on carbon suffers from sluggish reaction kinetics. As a result, a high charge potential (usually >4.2 V) is required to drive the partial decomposition of discharge products (e.g., Li_2CO_3) even at quite low currents, leading to large overpotential, low energy efficiency, poor reversibility, and quite limited cycling stability (10, 17, 18). Even though heteroatom doping (e.g., N, S, B, O) and defect engineering could facilitate the transformation of Li_2CO_3, it is still hard to achieve a charge potential of <4.0 V for carbon materials, and the corresponding energy efficiency of carbon-based Li-CO_2 batteries usually lies in the range of 60 to 70%. The large charge overpotential also causes a high risk of electrolyte decomposition and carbon corrosion, which suppresses the battery performance. To solve these problems, tremendous efforts have been devoted to exploring other kinds of materials that possess much higher catalytic activity than carbon materials. Recently, some metals/alloys (e.g., Ru (9, 19–21), Ir (22, 23), Ni (24), Fe (25, 26), Co (27), Cu (28, 29), RuCo (30), RuRh (31)) and metal compounds (e.g., Mo_2C (32, 33), VN (34), IrO_2 (35), RuP_2 (36), ZnS (37), MnO_x (38)) with abundant unoccupied orbits or dangling bonds have proven to be capable of enhancing the reaction kinetics of Li-CO_2 electrochemistry in aprotic organic electrolytes. In light of this point, most studies try to hybridize carbon materials with metals/alloys and/or metal compounds to fabricate composite catalysts for Li-CO_2 batteries with low overpotentials, focusing on

The authors declare no competing interest.

This article is a PNAS Direct Submission. J.M. is a Guest Editor invited by the Editorial Board.

[1]J.Z., T.W., L.C., and L.L. contributed equally to this work.

[2]To whom correspondence may be addressed. Email: zhanxi.fan@cityu.edu.hk or metzhao@ust.hk or l.gu@iphy.ac.cn or jianlicheng@caep.cn.

This article contains supporting information online at http://www.pnas.org/lookup/suppl/doi:10.1073/pnas.2204666119/-/DCSupplemental.

Published September 26, 2022.

regulating the morphology, size, composition, and distribution of metal-based components to promote the battery performance (7, 39). To date, the metal-based catalysts could decrease the charge potential of Li-CO_2 batteries to ~3.8 to 4.0 V and realize an energy efficiency of ~70 to 75%. However, although significant advances in Li-CO_2 batteries have been achieved by tuning the aforementioned factors, another important structural parameter of cathode catalysts (i.e., phase) is almost neglected in this direction.

In recent years, phase engineering of nanomaterials has emerged as an effective strategy to modulate the intrinsic physicochemical properties of materials, including the catalytic properties (40–45). Compared with the conventional phases, unusual phases possess different atomic arrangements. Consequently, the catalytic properties of materials could be significantly changed as the electronic structure is highly sensitive to atomic configuration (41). For instance, it was revealed that unusual hexagonal close-packed phases of Au (46–49) and Cu (50) nanomaterials exhibit much higher catalytic activity and selectivity than their conventional face-centered cubic (fcc) phase in the aqueous electrocatalytic CO_2 reduction reaction (CO_2RR). These observations suggest the great potential of unusual phase metal nanomaterials in next-generation catalysis-related energy storage and conversion applications (51), such as Li-CO_2 batteries. Therefore, despite that it puts forward strict requirements on the bifunctionality of cathode catalysts in aprotic Li-CO_2 batteries, tuning the round-trip reaction kinetics of the Li^+-mediated CO_2RR and CO_2 evolution reaction (CO_2ER) via the phase engineering of catalysts could be a feasible and promising strategy in boosting the electrochemical performance.

In this work, unconventional phase 4H/fcc Ir nanostructures are synthesized through controlled growth of Ir on 4H/fcc Au nanorods (NRs). As a proof-of-concept application, the obtained 4H/fcc Ir nanostructures are used as cathode catalysts in aprotic Li-CO_2 batteries. Compared with the Au substrate, the introduction of Ir nanostructures can facilitate the reversible formation of discharge products in Li-CO_2 electrochemistry. Significantly, unusual 4H/fcc Ir demonstrates much faster round-trip reaction kinetics than conventional fcc Ir in the Li^+-mediated CO_2RR and CO_2ER. It not only improves the discharge capacity and corresponding reversible capacity but it also decreases the discharge/charge overpotential remarkably, resulting in a low-charge plateau <3.61 V and high energy efficiency up to 83.8% during cycling. Ex situ/in situ studies and computational calculations reveal that the coordinative electron transfer via Ir-O coupling between 4H/fcc Ir and discharge products benefits the deep decomposition of low-crystalline/amorphous carbonates and carbon species. This study exhibits the high feasibility of using unconventional phase materials to further promote the electrochemical performance of nonaqueous metal-CO_2 batteries.

Results

Synthesis and Characterization. The synthesis of 4H/fcc Ir nanostructures on unusual phase Au NRs (denoted as Au@4H/fcc-Ir) is schematically illustrated in *SI Appendix*, Fig. S1 (see more details in *SI Appendix*, *Supplementary Methods*). Compared with the pristine 4H/fcc Au template (*SI Appendix*, Fig. S2), the NR surface became rough after Ir deposition (Fig. 1 *A* and *B*). The thickness of Ir nanostructures grown on the Au substrate was measured to be around 5 nm (*SI Appendix*, Fig. S3). The energy-dispersive X-ray spectrum (EDS) indicates an Au:Ir weight ratio of 0.86:0.14 in the obtained Au@Ir NRs (denoted as Au@4H/fcc-$Ir_{0.14}$), consistent with the inductively coupled plasma optical emission spectrometry analysis (*SI Appendix*, Fig. S4).

Spherical aberration-corrected high-angle annular dark-field scanning transmission electron microscopy (HAADF-STEM) was used to reveal the crystal structure of as-prepared Au@4H/fcc-$Ir_{0.14}$. The alternating distribution of 4H and fcc phases in Au core along the $[001]_{4H}/[111]_f$ close-packed directions was confirmed by the typical HAADF-STEM image and corresponding selected-area fast Fourier transform (FFT) patterns (Fig. 1 *C–E*). To investigate the crystal structure of Ir nanostructures, HAADF-STEM images of the edge areas on Au@4H/fcc-$Ir_{0.14}$ were collected. Along the close-packed directions of $[001]_{4H}/[111]_f$, the characteristic stacking sequences of "ABCB" and "ABC," which are attributed to 4H and fcc phases, respectively, can be clearly distinguished in the atomic-resolved images of Ir nanostructures (marked regions of Fig. 2*F* and *SI Appendix*, Fig. S5 *A–C*). The corresponding selected-area FFT patterns match well with the electron-diffraction patterns of fcc and 4H phases along the $[101]_f$ and $[110]_{4H}$ zone axes, respectively, indicating the coexistence of fcc and 4H phases in Ir nanostructures (Fig. 1 *G* and *H* and *SI Appendix*, Figs. S5 *D* and *E* and S6). In addition, from the enlarged HAADF-STEM image acquired along the $[110]_{4H}$ zone axis (Fig. 1*I*), the interplanar distances along the $[001]_{4H}$ close-packed direction of Au template and Ir nanostructure were measured at 2.31 and 2.19 Å, which are attributed to the $(004)_{4H\text{-}Au}$ and $(004)_{4H\text{-}Ir}$ planes, respectively (Fig. 1 *I* and *J*). Alternatively, the interplanar spacing of $(1\bar{1}0)_{4H\text{-}Ir}$ planes was measured at 2.38 Å. Based on these experimental results, the unit cell model of 4H Ir was built, in which the calculated unit cell parameters are a = 2.739 Å and c = 8.947 Å (Fig. 1*K*). For comparison, the unit cell model of fcc Ir is also provided, along with the crystal models of both 4H Ir and fcc Ir. In addition, HAADF-STEM images and the corresponding EDS line scanning and elemental mappings further corroborate the homogenous growth of Ir nanostructures on Au templates (Fig. 1 *L–Q*).

X-ray absorption near-edge structure (XANES) and extended X-ray absorption fine structure (EXAFS) spectroscopies were combined to reveal the electronic structure and coordination environment of Au@4H/fcc-$Ir_{0.14}$. As shown in Fig. 2*A*, in the Ir L_3-edge, the white line intensity, and XANES energy of 4H/fcc Ir match well with those of pure fcc Ir nanoparticles (NPs). The Fourier transforms of EXAFS spectra are provided to obtain the local structure of Ir (Fig. 2*B*). Both 4H/fcc Ir and fcc Ir show a dominant peak at ~2.52 Å in R space, corresponding to the Ir-Ir scattering path of the first shell (52). The smaller average Ir-Ir bond distance (*SI Appendix*, Fig. S7 and Table S1) and wider distribution of Ir-Ir bond length (Fig. 2*C*) in 4H/fcc Ir than those of fcc Ir indicate the formation of unusual Ir species (e.g., 4H Ir). In addition, the Ir-Ir coordination number (CN) of 4H/fcc Ir was calculated to be 9.1, which is much lower than that of pure fcc Ir (CN = 10.8). As for the Au L_3-edge, Au@4H/fcc-$Ir_{0.14}$ demonstrates almost the same white line intensity and XANES energy as those of the pristine 4H/fcc Au NRs (*SI Appendix*, Fig. S8*A*). Meanwhile, no apparent difference in the average Au-Au bond length was found between Au@4H/fcc-$Ir_{0.14}$ and 4H/fcc Au NRs (*SI Appendix*, Figs. S8*B* and S9 and Table S1). To further uncover the effect of the special coordination structure of 4H/fcc Ir and fcc Ir, the wavelet transforms (WTs) of Ir L_3-edge EXAFS were conducted. As shown in Fig. 2 *D* and *E*, 4H/fcc Ir nanostructures exhibit a much broader distribution of maximum intensity in

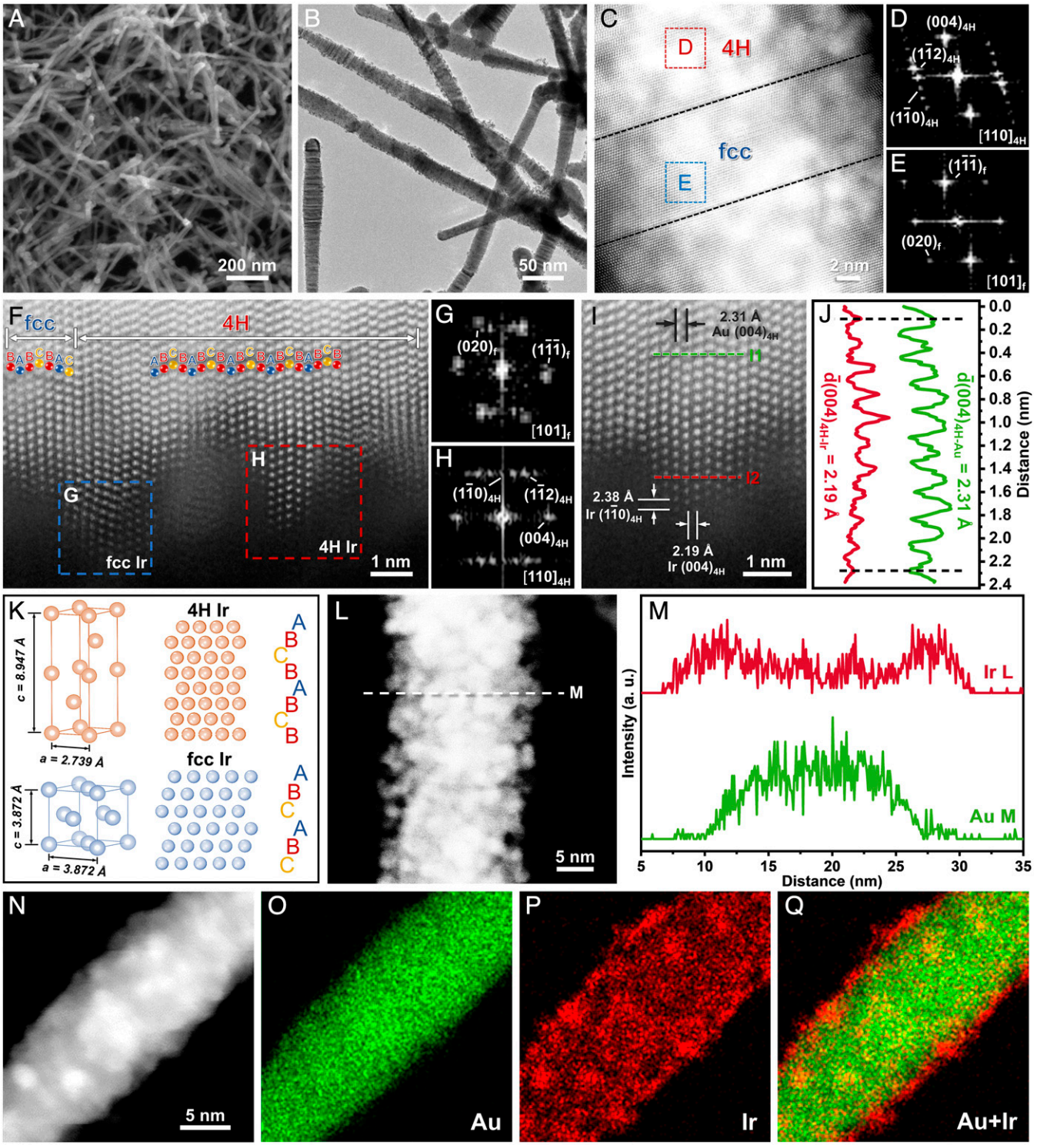

Fig. 1. Structural characterization of Au@4H/fcc-$Ir_{0.14}$ nanostructures. (*A* and *B*) SEM (*A*) and (*B*) TEM images of the as-synthesized Au@4H/fcc-$Ir_{0.14}$ nanostructures. (*C*) HAADF-STEM image of a single Au@4H/fcc-$Ir_{0.14}$ NR. (*D* and *E*) FFT patterns of the corresponding regions (*D* and *E*) marked in (*C*). (*F*) Aberration-corrected HAADF-STEM image acquired at the edge of the Au@4H/fcc-$Ir_{0.14}$ nanostructures. (*G* and *H*) FFT patterns of the corresponding regions (*G* and *H*) marked in (*F*). (*I*) Magnified HAADF-STEM image showing the lattice fringes of the inner 4H Au core and the outer 4H Ir nanostructure. (*J*) Integrated pixel intensities along the green (I1) and red (I2) dashed lines of the selected areas marked in (*I*). (*K*) Theoretical unit cell and crystal models of 4H (top panels) and fcc (bottom panels) Ir. (*L* and *M*) HAADF-STEM image (*L*) and the corresponding EDS line-scanning profile (*M*) across an individual Au@4H/fcc-$Ir_{0.14}$ NR indicated by the white dashed line in (*L*). (*N*–*Q*) HAADF-STEM image (*N*) and the corresponding EDS elemental mappings (*O*–*Q*) of the Au@4H/fcc-$Ir_{0.14}$.

the k range compared to pure fcc Ir NPs, which could be attributed to the diverse atomic arrangements of 4H Ir and fcc Ir (Fig. 1 *F*–*K*). In contrast, no evident change in the WT contour plots derived from Au L_3-edge EXAFS was observed, suggesting the good structure preservation of 4H/fcc Au after Ir deposition (*SI Appendix*, Fig. S8 *C* and *D*). In addition, X-ray photoelectron spectroscopy (XPS) was performed to further confirm the chemical states of Au@4H/fcc-$Ir_{0.14}$. From the high-resolution XPS spectrum of Ir 4f (Fig. 2*F*), two strong peaks corresponding to the $4f_{5/2}$ and $4f_{7/2}$ doublet of metallic Ir were found at 63.7 and 60.8 eV, while another couple of faint peaks at 65.6 and 62.0 eV indicate the slight oxidation of

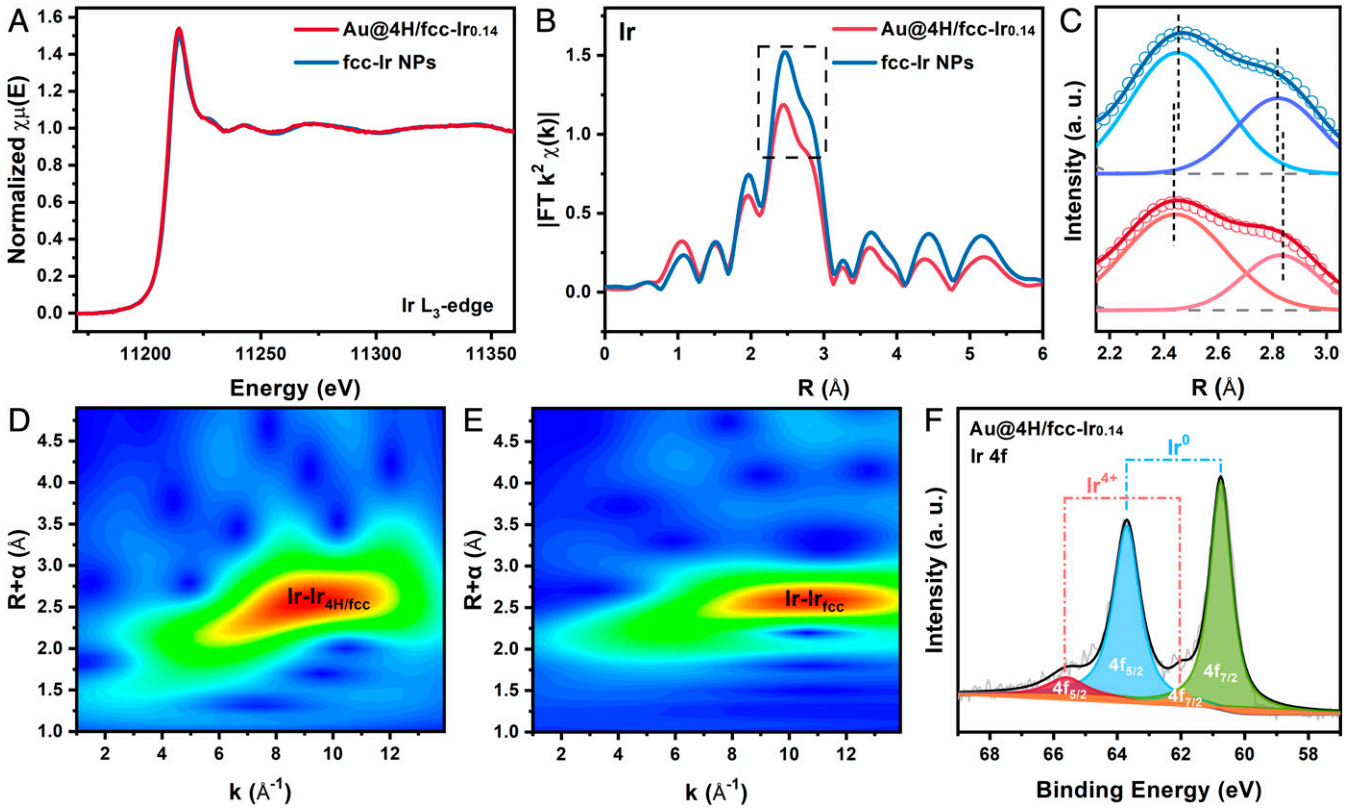

Fig. 2. X-ray spectral analysis of Au@4H/fcc-$Ir_{0.14}$ nanostructures. (*A*) XANES spectra at the Ir L_3-edge. (*B* and *C*) Fourier transform of Ir L_3 EXAFS spectra (*B*) and enlarged Fourier transform patterns (*C*) marked by the black dashed rectangle (in *B*) at R space of Au@4H/fcc-$Ir_{0.14}$ and fcc Ir NPs. (*D* and *E*) The counter plots of WT of Au@4H/fcc-$Ir_{0.14}$ (*D*) and fcc Ir NPs (*E*). (*F*) The high-resolution Ir 4f XPS spectrum of Au@4H/fcc-$Ir_{0.14}$.

Ir in air (22, 23). Simultaneously, only the peaks attributed to metallic Au can be recognized in the high-resolution XPS spectrum of Au 4f (*SI Appendix*, Fig. S10) (49).

The crystal structure of Ir nanostructures can be easily adjusted by controlling the thickness of Ir on the 4H/fcc Au template. In general, with the increase in Ir thickness, the Au template gradually cannot confine the growth of unusual phase Ir, leading to the formation of fcc-rich nanocrystals in the outer layer of Ir nanostructures. In specific, another two kinds of Au@4H/fcc-Ir NRs were synthesized by the same method but with increased amounts of Ir precursor and extended growth time. The Au:Ir weight ratios in these two samples were measured at 82:18 (denoted as Au@4H/fcc-$Ir_{0.18}$) and 75:25 (denoted as Au@4H/fcc-$Ir_{0.25}$), respectively (*SI Appendix*, Figs. S11*A* and S12*A*). As shown in *SI Appendix*, Fig. S11 *B* and *C*, the thickness of Ir in Au@4H/fcc-$Ir_{0.18}$ is ∼7 nm, resulting in the distinct decrease in 4H-phase content in Ir nanostructures. As for Au@4H/fcc-$Ir_{0.25}$, the outer layer of Ir nanostructures with a thickness of ∼12 nm is almost full of fcc Ir nanocrystals (*SI Appendix*, Fig. S12 *B–E*).

Electrochemical Performance of Li-CO_2 Batteries. The as-synthesized Au@4H/fcc-Ir NRs were used as cathode catalysts to investigate the effect of phase on the reaction kinetics of Li^+-mediated nonaqueous CO_2RR and CO_2ER in Li-CO_2 batteries (Fig. 3*A*). Since Au is an eligible substrate for Li-CO_2 electrochemistry, no other carbon additives (e.g., super P (9), Ketjen black (10), Vulcan XC72 (31)) were added into the catalyst system. Thus, Au excludes the interference by carbon species that are active catalysts for Li-CO_2 batteries (9, 10, 31). In addition, dimethyl sulfoxide (DMSO) with a high donor number (DN) of 29.8 was used as the electrolyte solvent in this work. Note that the limited specific surface active sites of metal catalysts usually require a higher CO_2 concentration near the surface region than carbon-based counterparts to trigger the redox reactions (53–56). Galvanostatic discharge and charge tests were conducted on different Ir cathodes toward Li-CO_2 electrochemistry. To measure the performance of pure fcc Ir, the control cathode catalysts were prepared by physically mixing 4H/fcc Au NRs and fcc Ir NPs with a weight ratio of 86:14 (denoted as Au + fcc-$Ir_{0.14}$, *SI Appendix*, Fig. S13). All of the current densities and capacities were normalized to the mass of Ir. The curtailing capacity was set at 500 mAh g^{-1}_{Ir} on account of the large mass density of Ir, which is 10 times larger than that of carbon, as well as the general test conditions used in metal-gas systems. The mass loadings of Ir were kept at a similar level on different cathodes. Before the measurements, the negligible contributions by Li intercalation and pseudocapacitance were first confirmed by the nonevident capacities on Au and Au/Ir cathodes in Ar (*SI Appendix*, Fig. S14). Hence, almost all of the capacities recorded should originate from the Li-CO_2 electrochemistry.

Rate capability is an important indicator for reaction kinetics (57, 58). As shown in Fig. 3*B*, with the increase in current density from 50 to 100, 250, and 500 mA g^{-1}_{Ir} on Au@4H/fcc-$Ir_{0.14}$, the discharge voltage shows a slight decrease, but the charge potential polarization gradually increases, with the charge termination voltage moving upward from 3.61 to 3.80, 3.92, and 4.12 V, respectively. In comparison, Au + fcc-$Ir_{0.14}$ suffers from much serious voltage polarization at every applied current density (Fig. 3*C* and *SI Appendix*, Fig. S15 *A–D*). Importantly, Au@4H/fcc-$Ir_{0.14}$ demonstrates much lower discharge and charge overpotential than Au + fcc-$Ir_{0.14}$ under the current densities of 50 to 500 mA g^{-1}_{Ir} (*SI Appendix*, Fig. S15*E*). The better rate capability of Au@4H/fcc-$Ir_{0.14}$ than

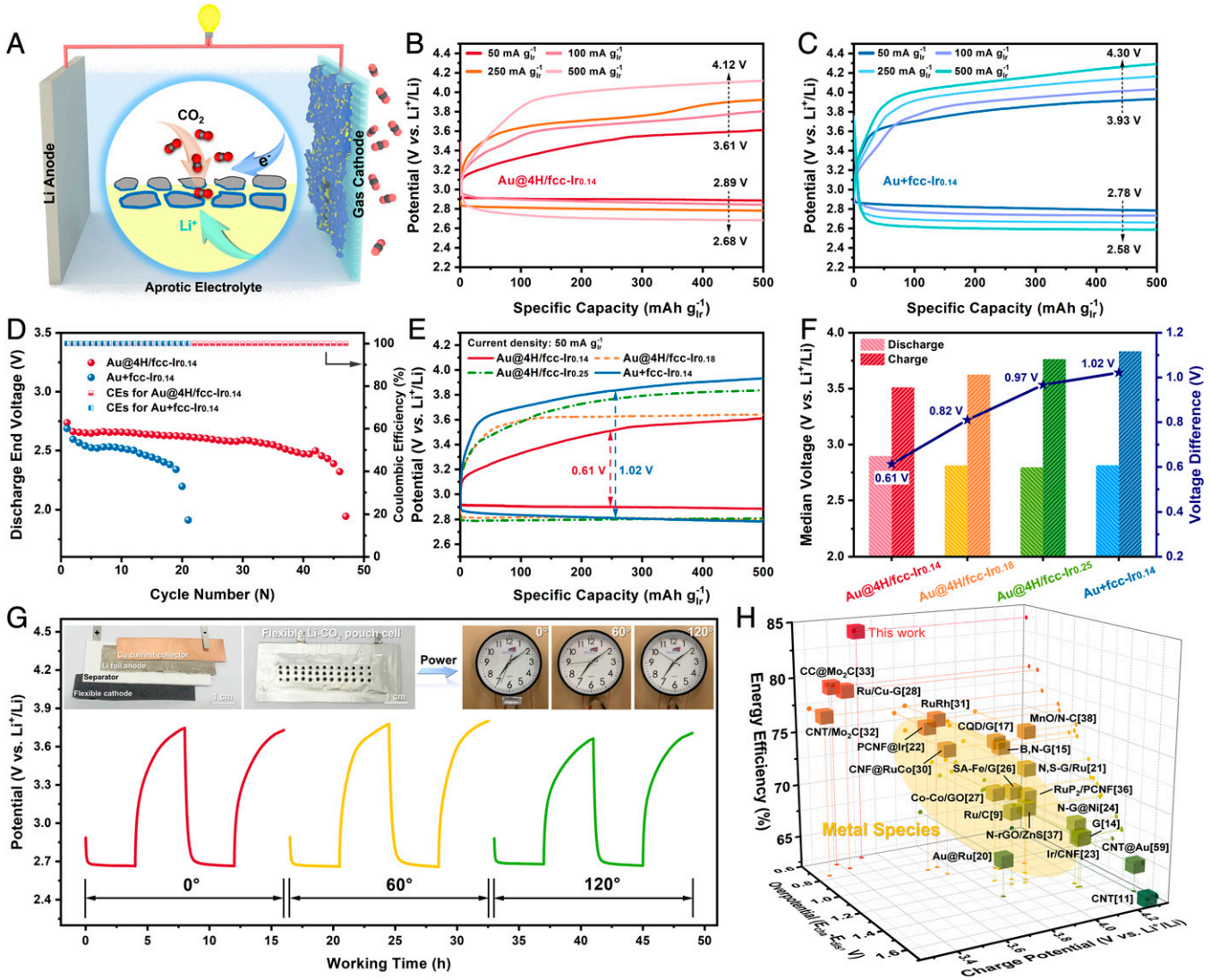

Fig. 3. Electrochemical performance of the assembled aprotic Li-CO_2 batteries. (*A*) Schematic illustration depicting the general configuration and working mechanism of aprotic Li-CO_2 batteries. (*B* and *C*) Rate capabilities of Au@4H/fcc-$Ir_{0.14}$ (*B*) and Au + fcc-$Ir_{0.14}$ (*C*) cathodes. (*D*) Long-term cycling stability of Au@4H/fcc-$Ir_{0.14}$ and Au + fcc-$Ir_{0.14}$ at 500 mA g^{-1}_{Ir} and 500 mAh g^{-1}_{Ir}. (*E* and *F*) Discharge-charge profiles at 50 mA g^{-1}_{Ir} within 500 mAh g^{-1}_{Ir} (*E*) and comparison of the median discharge/charge voltages and voltage differences (*F*) of Au@4H/fcc-Ir and Au + fcc-$Ir_{0.14}$. (*G*) Discharge-charge profiles of a flexible Li-CO_2 pouch cell using Au@4H/fcc-$Ir_{0.14}$ at various bending angles at 50 μA within 200 μAh, along with the digital photographs of a clock powered by this device as insets. (*H*) Comparison on the charge potential, overpotential, and energy efficiency of as-synthesized Au@4H/fcc-$Ir_{0.14}$ and other representative catalysts for Li-CO_2 batteries reported previously.

Au + fcc-$Ir_{0.14}$ indicates the faster CO_2RR and CO_2ER kinetics. To reveal the ability of sustaining fast reaction kinetics by Ir catalysts, long-term cycling behaviors were investigated at a high rate of 500 mA g^{-1}_{Ir} and a curtailing capacity of 500 mAh g^{-1}_{Ir}. From Fig. 3*D* and *SI Appendix*, Fig. S16, Au@4H/fcc-$Ir_{0.14}$ show the longer working lifespan of 46 cycles than that of Au + fcc-$Ir_{0.14}$ (20 cycles), along with the lower overpotential and more stable discharge/charge profiles. The cycling life of Au@4H/fcc-$Ir_{0.14}$ can be further extended above 60 cycles under 250 mA g^{-1}_{Ir} and 250 mAh g^{-1}_{Ir} (*SI Appendix*, Fig. S17). The performance decay probably originates from the instability of the 4H/fcc Au substrate and metal anode corrosion in aprotic Li-CO_2 batteries using DMSO-based electrolytes. Note that pure Au cathodes can only work for 4 cycles even under mild conditions (*SI Appendix*, Fig. S18). In addition, as evidenced by the discharge/charge profiles and median discharge/charge potentials at 250 mA g^{-1}_{Ir} and 500 mAh g^{-1}_{Ir}, Au@4H/fcc-$Ir_{0.14}$ can maintain relatively high energy efficiencies even at high rates (*SI Appendix*, Fig. S19).

The electrochemical behaviors of Au@4H/fcc-Ir and Au + fcc-$Ir_{0.14}$ toward Li-CO_2 electrochemistry were compared to further reveal the phase effect of Ir nanostructures. As shown in Fig. 3*E*, the discharge-charge voltage gaps exhibit an increasing trend with the decrease in 4H-phase content in Ir nanostructures at 50 mA g^{-1}_{Ir} and 500 mAh g^{-1}_{Ir}. Fig. 3*F* demonstrates the detailed discharge/charge plateaus and corresponding voltage gaps of the Ir nanostructures. Remarkably, Au@4H/fcc-$Ir_{0.14}$ exhibits the median discharge and charge potentials at ~2.90 and 3.52 V, respectively, resulting in the lowest discharge-charge voltage difference of 0.61 V and the highest energy efficiency of 83.8% among all of the measured catalysts (0.82 V/78.2% for Au@4H/fcc-$Ir_{0.18}$, 0.97 V/75.6% for Au@4H/fcc-$Ir_{0.25}$, and 1.02 V/74.2% for Au + fcc-$Ir_{0.14}$). Moreover, the charge termination voltage of Au@4H/fcc-$Ir_{0.14}$ is <3.61 V. As for Au@4H/fcc-$Ir_{0.25}$, the discharge/charge profiles are approaching those of Au + fcc-$Ir_{0.14}$. Given the fact that the surface of Au@4H/fcc-$Ir_{0.25}$ is mainly covered by fcc Ir nanostructures and metal-gas electrochemistry is more sensitive

to the surface state of catalysts, it is reasonable that 4H/fcc-$Ir_{0.25}$ exhibits a discharge-charge behavior that is very similar to that of pure fcc Ir. The aforementioned results suggest that the unconventional 4H phase of Ir tends to favor the Li^+-mediated CO_2RR and CO_2ER kinetics in aprotic Li-CO_2 batteries over that of the common fcc counterparts.

In addition, a flexible Li-CO_2 pouch cell was constructed using Au@4H/fcc-$Ir_{0.14}$ as the cathode catalyst. As shown in Fig. 3*G*, the fabricated pouch cell exhibits an excellent electrochemical behavior retention under various bending angles, ranging from 0° to 60° and 120°. The as-fabricated pouch cell is also able to provide electricity steadily for a commercial clock even during the continuous deformation process (illustrations within Fig. 3*G* and *SI Appendix*, Movie S1). The successful demonstration of flexible Li-CO_2 pouch cells indicates the great potential of using unconventional phase nanomaterials to promote the round-trip reaction kinetics of flexible metal-gas batteries in practical application scenarios.

To better elucidate the advantages of unusual Au@4H/fcc-$Ir_{0.14}$ nanostructures for aprotic Li-CO_2 batteries, a systematic comparison including the charge potential, overpotential, and energy efficiency has been made between this work and other representative metal-based catalysts that were reported previously. As shown in Fig. 3*H*, Au@4H/fcc-$Ir_{0.14}$ nanostructures demonstrate the highest energy efficiency among all of the listed catalysts. Furthermore, to the best of our knowledge, there are few metal/alloy-based catalysts that can reach such a low charge voltage (i.e., <3.61 V) (*SI Appendix*, Table S2). Note that at least ~3.75 V is typically required to drive the decomposition of discharge products on previously reported catalysts (9, 20, 22, 31, 33, 59).

Electrochemical Reaction Mechanism. Ex situ and in situ techniques were combined to explore the reason why unusual 4H/fcc Ir is able to boost the CO_2 reduction and evolution kinetics in aprotic Li-CO_2 batteries. Here, cyclic voltammetry (CV) was used to reveal the potential and current differences on the above redox reactions. To evaluate the performance of intrinsic Li-CO_2 electrochemistry occurring on the Au substrate and make a reasonable performance comparison under the equivalent conditions, the specific capacities and current densities were normalized to the total weight of metal (i.e., Au and Ir). As shown in Fig. 4*A* and *SI Appendix*, Fig. S20, Au@4H/fcc-$Ir_{0.14}$ shows the larger current density and lower reaction overpotential of CO_2RR and CO_2ER than those on the bare Au substrate and Au + fcc-$Ir_{0.14}$, which means it could allow the faster reaction kinetics. In the following, deep discharge/charge behaviors of Au, Au + fcc-$Ir_{0.14}$ and Au@4H/fcc-$Ir_{0.14}$ cathodes were also investigated. On account of the large mass content of the Au substrate, the applied current density of 50 mA g^{-1}_{metal} (approximately

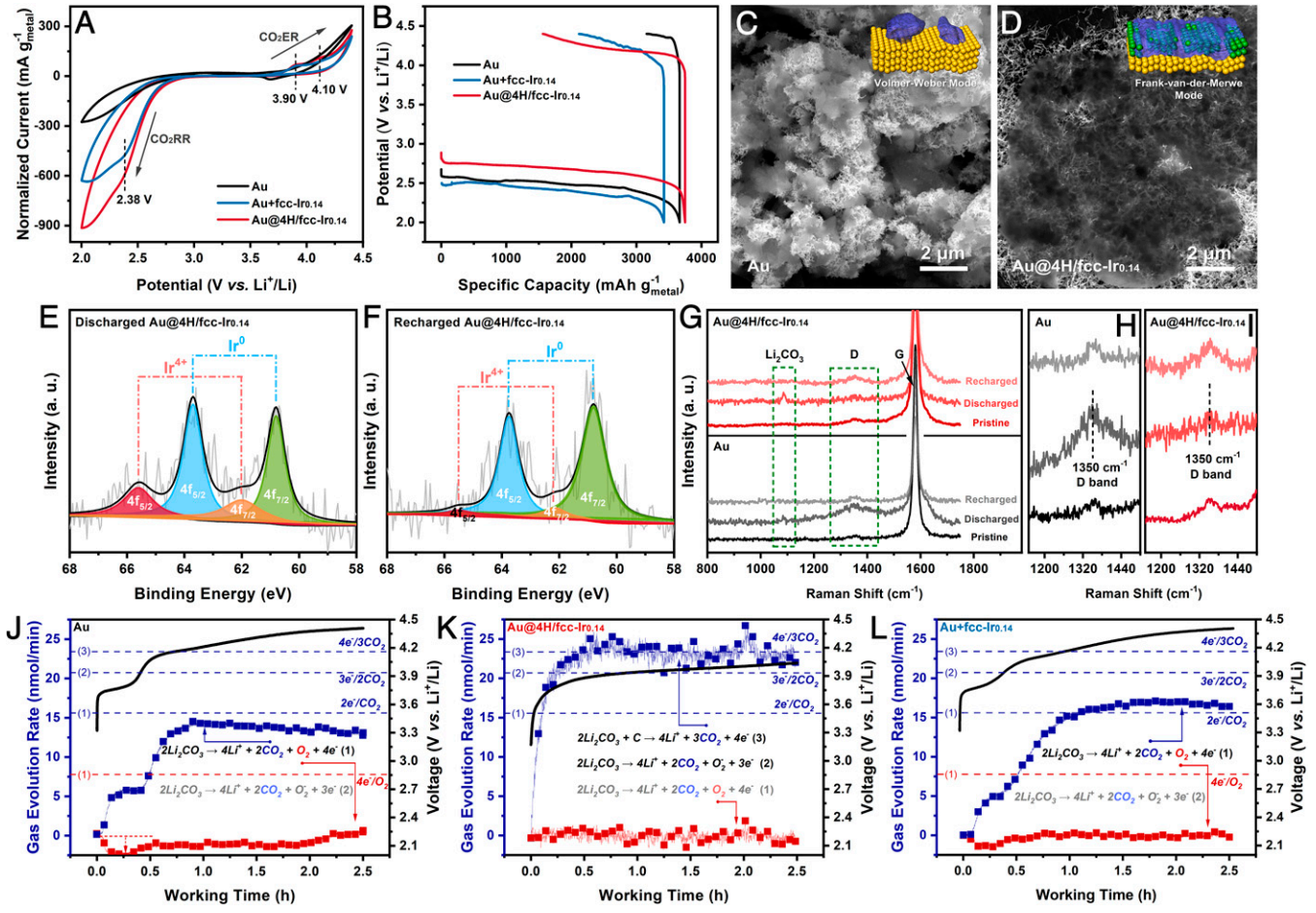

Fig. 4. Ex situ/in situ studies on the underlying reaction mechanism of different Li-CO_2 electrochemistry. (*A* and *B*) CV curves at 0.2 mV s^{-1} (*A*) and galvanostatic discharge-charge profiles at 50 mA g^{-1}_{metal} (*B*) of Au, Au + fcc-$Ir_{0.14}$ and Au@4H/fcc-$Ir_{0.14}$ over the potential window of 2.0 to 4.4 V in CO_2. (*C* and *D*) Typical SEM images of discharge products formed on the Au substrate (*C*) and Au@4H/fcc-$Ir_{0.14}$ (*D*), along with the illustrations of different growth modes of discharge products as insets. (*E* and *F*) The high-resolution Ir 4f XPS spectra of Au@4H/fcc-$Ir_{0.14}$ cathodes at the first discharged state (*E*) and the first recharged state (*F*). (*G–I*) Raman spectra of Au@4H/fcc-$Ir_{0.14}$ and bare Au cathodes at different electrochemical states. (*J–L*) In situ DEMS patterns and the corresponding charge profiles of Au substrate (*J*), Au@4H/fcc-$Ir_{0.14}$ (*K*), and Au + fcc-$Ir_{0.14}$ (*L*) at 50 μA, respectively.

equal to 350 mA g^{-1}_{Ir}) would cause a high reaction rate, which easily leads to the rapid voltage polarization that shuts down the battery. As shown in Fig. 4*B*, despite the higher working voltage plateau at ~2.7 V, Au@4H/fcc-$Ir_{0.14}$ demonstrates a deep discharge specific capacity of 3,748.3 mAh g^{-1}_{metal} at the current density of 50 mA g^{-1}_{metal}, which is even slightly higher than that of the pristine Au substrate (3,665.1 mAh g^{-1}_{metal}). Significantly, the Li-CO_2 electrochemistry occurring on the pure Au substrate shows poor reversibility, only exhibiting a low Coulombic efficiency (CE) of 13.90%. In comparison, the reversible capacities of 1,304.6 and 2,187.9 mAh g^{-1}_{metal} were achieved by Au + fcc-$Ir_{0.14}$ and Au@4H/fcc-$Ir_{0.14}$, corresponding to the high CEs of 38.11% and 58.37%, respectively. These results indicate that 4H/fcc Ir should not only facilitate the conversion of CO_2 to carbonates but also improve the decomposition and reversibility of discharge products.

The morphology evolution of Au@4H/fcc-$Ir_{0.14}$ and Au cathodes was checked at different discharge and recharge states. After the first discharge process, large-sized aggregates of discharge products are discretely distributed in the Au cathode (Fig. 4*C*), while the discharge products exist as a continuous film covering catalysts in the Au@4H/fcc-$Ir_{0.14}$ cathode (Fig. 4*D*). This is attributed to the different growth modes of discharge products in the aforementioned Li-CO_2 batteries (*SI Appendix*, Fig. S21). If the growth process dominates (usually in the case of inadequate catalytic sites and/or lower catalytic activity), the newly generated discharge products (e.g., Li_2CO_3 and C) tend to accumulate on the surface of preformed ones, leading to the formation of many isolated aggregates along the Volmer-Weber mode (51, 54, 55). On the contrary, if the nucleation process dominates (usually in the case of abundant catalytic sites and/or higher catalytic activity), then there are more active surfaces available for the homogeneous nucleation of newly generated discharge products, resulting in the generation of continuous film along the Frank-van der Merwe mode (51, 54, 55). Owing to the larger contact area and stronger interaction between catalysts and discharge products, the latter mode is in favor of the lower CO_2RR energy barrier (higher working voltage) and larger storage space for discharge products (larger specific capacity) in Li-CO_2 cells using Au@4H/fcc-$Ir_{0.14}$. Simultaneously, the latter mode can also promote the decomposition of discharge products, as evidenced by the scanning electron microscopy (SEM) observations (*SI Appendix*, Fig. S22). Moreover, after recharging, the initial morphology and structure of Au@4H/fcc-$Ir_{0.14}$ catalyst can be well preserved (*SI Appendix*, Fig. S23).

XPS was used to investigate the chemical state evolution of Ir and Au during cycling. Unexpectedly, apart from the common valence variation of Li_2CO_3 in the cathodes (*SI Appendix*, Figs. S24 and S25), it was observed that the intensity of peaks corresponding to the oxidized state of Ir increases remarkably after the initial discharge process and then decreases to pristine status after the subsequent recharge process (Fig. 4 *E* and *F*), while the chemical state of Au remained the same during the cycling (*SI Appendix*, Fig. S26) (60). It suggests that there should be some coordinative electron transfer between 4H/fcc Ir and discharge products through the Ir-O coupling during discharging (32, 33). Upon recharging, the Ir-O coupling was broken with the gradual decomposition of discharge products, and simultaneously, the delocalized electrons of Ir atoms returned to 4H/fcc Ir. However, this kind of electron transfer phenomenon cannot be detected in the pure Au cathodes (*SI Appendix*, Fig. S27) and Au + fcc-$Ir_{0.14}$ cathodes (*SI Appendix*, Fig. S28). The detailed reaction process occurring on cathodes during cycling was elucidated by Raman spectra (Fig. 4*G*). A stretching peak at ~1,085 cm^{-1}, which is ascribed to the C-O bond of Li_2CO_3, appeared after discharging (20, 26). The broadened full wave at half-maximum (~20 cm^{-1} for Au@4H/fcc-$Ir_{0.14}$ versus 12 cm^{-1} for Au) suggested that the crystallinity of Li_2CO_3 formed on Au@4H/fcc-$Ir_{0.14}$ is lower than that on Au (*SI Appendix*, Fig. S29). The low-crystalline Li_2CO_3 was more easily decomposed under a relatively low charge potential, given that no obvious peak of Li_2CO_3 can be recognized on Au@4H/fcc-$Ir_{0.14}$ after recharging (61). A similar phenomenon was observed for carbon, another kind of discharge product in the Li-CO_2 battery. From the magnified Raman spectra around the D band of carbon species (~1,350 cm^{-1}), Au@4H/fcc-$Ir_{0.14}$ exhibited a much broader and weaker peak compared with Au after discharging, indicating the generated carbon is mostly amorphous or of low crystallinity (62, 63). Upon recharging, the peak of the D band returned to the pristine state in the Au@4H/fcc-$Ir_{0.14}$ cathode, while this peak became a little bit stronger than the initial state in the Au cathode. These observations indicate that Li_2CO_3 and carbon should be largely decomposed in the Au@4H/fcc-$Ir_{0.14}$ cathode, but there are some detectable residuals in the Au cathode after recharging.

In situ differential electrochemical mass spectrometry (DEMS) was further used to reveal the underlying CO_2ER mechanism of Li-CO_2 electrochemistry with different catalysts. The electrochemical behaviors of reactions occurring on the Au substrate can be regarded as the intrinsic properties of aprotic Li-CO_2 electrochemistry, given that Au is a commonly used platform allowing metal-gas electrochemistry in spectroscopy-related studies (20, 64). According to Fig. 4*J*, the balanced CO_2 evolution rate profile on the Au cathode is close to but below the standard line [**1**] ascribed to $2e^-/CO_2$ (charge-to-mass ratio) and the corresponding charge potential reaches around 4.3 V, which indicates the partial decomposition of Li_2CO_3 via (20, 65)

$$2Li_2CO_3 \rightarrow 4Li^+ + 2CO_2 + O_2 + 4e^-, \qquad [1]$$

even under such a high overpotential. This is due to the insulating and thermodynamically stable characteristics of discharge products generated on Au with poor catalytic activity. Although it does not produce O_2^- radicals with the strong oxidizing power via another decomposition pathway based on $3e-/2CO_2$ via

$$2Li_2CO_3 \rightarrow 4Li^+ + 2CO_2 + O_2^- + 3e^-, \qquad [2]$$

the generated O_2 may be still sufficient to oxidize the nanoscale Au substrate, limiting the cycling stability of Au cathode to ≤4 cycles. The slight Au oxidation was also verified by the weak oxygen consumption at the initial charge stage, which becomes much more obvious at the third charge process (*SI Appendix*, Fig. S30). After the introduction of Ir (no matter whether 4H/fcc or pure fcc Ir) to the Au substrate, the electrophilicity and nucleophilicity of catalysts are improved through the stronger electron interaction between Ir and reactive precursors/discharge products, thereby decreasing the round-trip reaction overpotential and increasing the reversibility of Li-CO_2 electrochemistry. This statement can be supported further by the reduced charge profiles shown in Fig. 4 *K* and *L*. The balanced CO_2 evolution rate profiles corresponding to Au@4H/fcc-$Ir_{0.14}$ and Au + fcc-$Ir_{0.14}$ lie in the range of the standard line [**2**] representing $2e^-/CO_2$ to the standard line [**3**] representing $4e-/3CO_2$ via

$$2Li_2CO_3 + C \rightarrow 4Li^+ + 3CO_2 + 4e^-, \qquad [3]$$

suggesting the enhanced reaction kinetics in both Ir-based Li-CO_2 batteries. Significantly, the real charge-to-mass ratio of Au@

4H/fcc-$Ir_{0.14}$ was calculated to be 1.39 e^-/CO_2, which is much better than that of Au + fcc-$Ir_{0.14}$ (2.38 e^-/CO_2) and even approaches the ideal value of 1.33 e^-/CO_2 along the completely reversible pathway (see the detailed calculation methods in the *SI Appendix*). This phenomenon indicates that carbon degradation has also been deeply activated in the 4H/fcc Ir-based Li-CO_2 cell. The aforementioned results suggest that compared with fcc Ir, the more reversible formation of amorphous/low-crystalline discharge products on unusual 4H/fcc Ir leads to the boosted round-trip reaction kinetics (*SI Appendix*, Fig. S31).

Computational Calculations. First-principles calculations based on density functional theory (DFT) were performed to gain some theoretical insights into the excellent catalytic activity of unusual phase Ir toward Li^+-mediated CO_2RR and CO_2ER. In the first place, phonon spectra were simulated to verify the dynamic stability of the 4H Ir crystal obtained by the CALYPSO (66). The results show that 4H Ir lacks imaginary models and thus possesses a good dynamical stability (*SI Appendix*, Fig. S32*A*). Band structure calculations further demonstrate that 4H Ir maintains the typical metallic property, analogous to fcc Ir (*SI Appendix*, Fig. S32 *B* and *C*). Because a high-DN solvent (i.e., DMSO) is required to enable the 4-electron transfer Li-CO_2 electrochemistry ($4Li + 3CO_2 \leftrightarrow 2Li_2CO_3 + C$) using pure metal catalysts, the solution pathway should dominate in CO_2 reduction, according to the previous relevant studies involving metal-gas batteries (53–56). Hence, the wettability of catalyst surface toward the reaction precursors and discharge products remarkably affects the position and rate of the reaction equilibrium (CO_2RR kinetics). From the precursor side, we calculated the adsorption energies of Li atom (E_{ads}(Li)) and CO_2 molecule ($E_{ads}(CO_2)$) on the thermodynamically stable (111) surface of fcc Ir and 3 mainly exposed (004), (1$\bar{1}$0), (110) surfaces of the 4H Ir nanostructures. The E_{ads}(Li) on $(004)_{4H}$, $(1\bar{1}0)_{4H}$, and $(110)_{4H}$ facets reach 2.97, 2.96, and 3.05 eV, respectively, which are much higher than that (2.69 eV) on the $(111)_f$ facet (*SI Appendix*, Fig. S33 *A*, *D*, *G*, and *J* and Table S3). In terms of CO_2 adsorption, although $(004)_{4H}$ and $(1\bar{1}0)_{4H}$ facets show $E_{ads}(CO_2)$ similar to that (0.03 eV) of the $(111)_f$ facet, $E_{ads}(CO_2)$ on the $(110)_{4H}$ facet (0.77 eV) is an order of magnitude larger than that of the $(111)_f$ facet (*SI Appendix*, Fig. S33 *B*, *E*, *H*, and *K* and Table S3). Therefore, it is believed that 4H Ir has better wettability toward the reaction precursors, which enlarges the concentration of Li^+ and CO_2 near the catalyst surface and thereby promotes the positive shift of the equilibrium.

From the product side, we further considered the interactions between Li_2CO_3 (the dominant discharge product) and the aforementioned four types of Ir surfaces. According to the calculated adsorption energies of Li_2CO_3 ($E_{ads}(Li_2CO_3)$), it was deduced that the $(1\bar{1}0)_{4H}$ and $(110)_{4H}$ facets of 4H Ir should be preferable for electrocatalytic CO_2 reduction, on account of their superior compatibility to Li_2CO_3 (2.64 eV for $(1\bar{1}0)_{4H}$ and 2.28 eV for $(110)_{4H}$, while 1.64 eV for $(111)_f$), as shown in *SI Appendix*, Fig. S33 *C*, *F*, *I*, and *L* and Table S3. The larger $E_{ads}(Li_2CO_3)$ suggests that it would be much easier and faster for 4H Ir than fcc Ir to capture Li_2CO_3 generated by the solution pathway, which will decrease the discharge product concentration at the electrochemically active regions for CO_2RR and thus further make the equilibrium move forward as well as boost the kinetics. Moreover, the partial electronic density of states (PDOS) (Fig. 5*A* and *SI Appendix*, Fig. S34) and charge density differences (Fig. 5 *B*–*D*) reveal that the interactions between Li_2CO_3 and four types of Ir surfaces are mainly via the Ir-O bond. Compared with the $(111)_f$ facet, there are much larger coupling regions between Ir and O atoms in PDOS when a Li_2CO_3 molecule is adsorbed on $(1\bar{1}0)_{4H}$ and $(110)_{4H}$ facets, explaining why the $E_{ads}(Li_2CO_3)$ is enhanced on the latter two surfaces. Bader charge analysis elucidates that there is 0.5084 e^- transfer between the Li_2CO_3 molecules and Ir atoms for the $(1\bar{1}0)_{4H}$ facet, while this value was

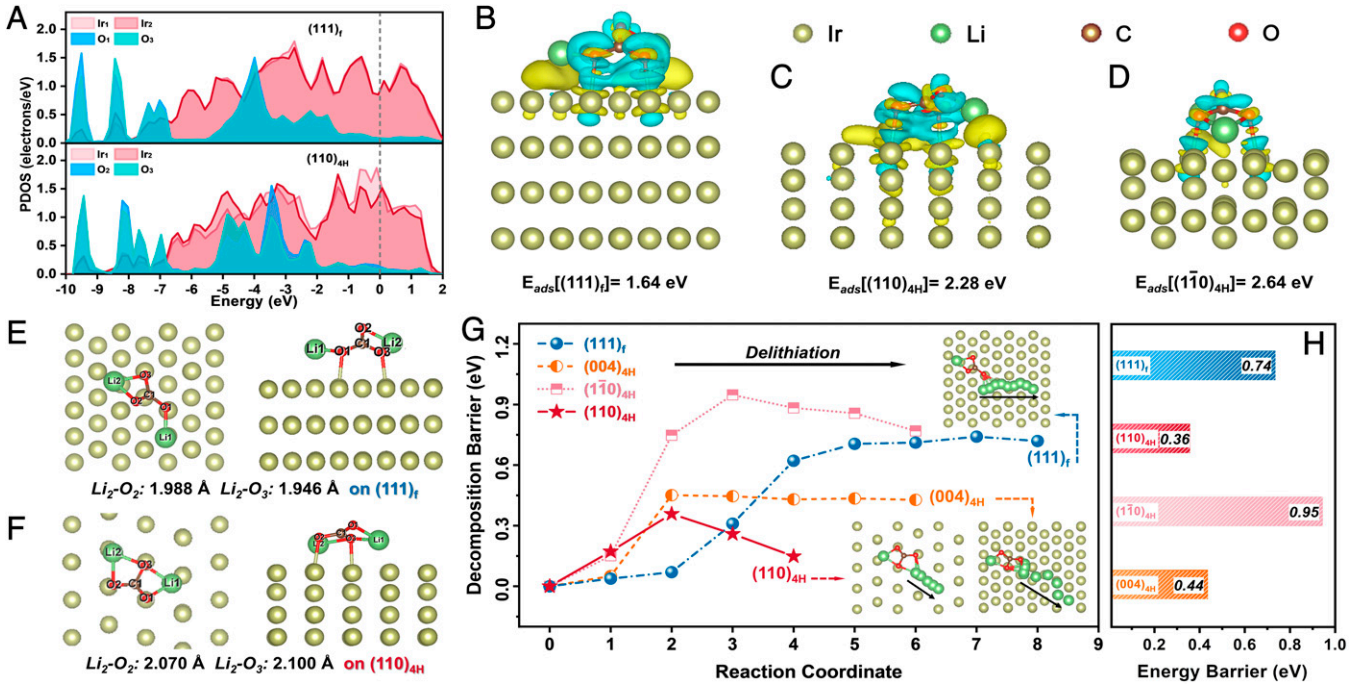

Fig. 5. Theoretical calculations depicting the difference on modulating the Li^+-mediated CO_2RR and CO_2ER kinetics by 4H Ir and fcc Ir. (*A*) The PDOS around the Fermi level (E_f) of $(111)_f$ and $(110)_{4H}$ facets of Ir after Li_2CO_3 was adsorbed. (*B*–*D*) Bader charge density difference of Li_2CO_3 adsorbed on $(111)_f$ (*B*), $(110)_{4H}$ (*C*), and $(1\bar{1}0)_{4H}$ (*D*) facets of Ir. (*E* and *F*) Top views (left panels) and side views (right panels) of the optimized energetically most favorable structures of Li_2CO_3 adsorbed on $(111)_f$ (*E*) and $(110)_{4H}$ (*F*) surfaces of Ir. (*G* and *H*) The dynamic simulations (*G*) and corresponding maximum energy barriers (*H*) during the decomposition of Li_2CO_3 on $(111)_f$, $(004)_{4H}$, $(1\bar{1}0)_{4H}$, and $(110)_{4H}$ facets of Ir.

only 0.4393 e^- for the $(111)_f$ facet (*SI Appendix*, Table S3). It further suggests that the electronic interaction via Ir-O coupling is much stronger for 4H Ir than fcc Ir. This is also consistent with the XPS results, in which the content of Ir oxidation state in Au@4H/fcc-$Ir_{0.14}$ increases after discharging (Fig. 4 *E* and *F*).

The CO_2ER is equally as important as CO_2RR in metal-CO_2 batteries. To evaluate the kinetic differences of Li_2CO_3 oxidation during the charging process, we also simulated the dynamic decomposition of Li_2CO_3 on the aforementioned four Ir surfaces. The decomposition process from an intact Li_2CO_3 molecule into a $LiCO_3$ cluster and a single Li ion was considered at the initial dissociation stage of discharge products, corresponding to the fracture of a Li-O bond. Because the lengths of the two Li-O bonds, which are initially equal in the Li_2CO_3 molecule, will change after Li_2CO_3 is adsorbed on the surfaces, the decomposition processes are always fixed on the Li_2-O bond with the largest bond length and hence the lowest bond energy. It is also noteworthy that the average Li-O bond lengths of Li_2CO_3 on the $(1\bar{1}0)_{4H}$ and $(110)_{4H}$ surfaces are distinctly larger than the counterparts on the $(111)_f$ surface (Fig. 5 *E* and *F* and *SI Appendix*, Fig. S35), suggesting the lower structural stability of Li_2CO_3 generated on 4H Ir than that on fcc Ir. The dynamic dissociation processes of the first Li atom in Li_2CO_3 were further simulated on the aforementioned four kinds of Ir surfaces, as shown in Fig. 5*G*. Specifically, the highest decomposition energy barriers of Li_2-O bonds are 0.74, 0.36, 0.95, and 0.44 eV on the $(111)_f$, $(110)_{4H}$, $(1\bar{1}0)_{4H}$, and $(004)_{4H}$ facets, respectively (Fig. 5*H*). This indicates that 4H Ir is more favorable for Li_2CO_3 dissociation than the fcc Ir, thereby allowing faster CO_2ER kinetics.

In addition, to further confirm the origin of lower discharge-charge overpotentials by unusual phase Ir, DFT calculations on the Au substrates were also performed. It was found that 4H Au possesses more lithiophilic surfaces than fcc Au, but the discrepancies of $E_{ads}(CO_2)$, $E_{ads}(Li_2CO_3)$, electron transfer, and Li-O bond length of Li_2CO_3 on different crystal phases of Au are not so obvious (*SI Appendix*, Figs. S36–S38 and Table S4). The dynamic delithiation simulations further reveal that the decomposition energy barriers of Li_2CO_3 on the four different surfaces of Au are similar and range from 1.35 to 1.58 eV (*SI Appendix*, Fig. S39), much larger than those observed on Ir surfaces. The above simulation results not only explain why Ir can enhance the Li^+-mediated CO_2RR and CO_2ER kinetics but also suggest that Li-CO_2 based reactions should have analogous electrochemical behaviors on 4H or fcc Au surfaces, highlighting the great significance of unusual phase Ir nanostructures in promoting the aprotic Li-CO_2 electrochemistry.

Discussion

In summary, unusual phase 4H/fcc Ir nanostructures have been successfully synthesized by controlling the growth of Ir on the 4H/fcc Au template. Significantly, 4H/fcc Ir demonstrated superior catalytic performance over fcc Ir in facilitating the Li^+-mediated CO_2RR and CO_2ER kinetics in the aprotic Li-CO_2 battery. It not only can enhance the full specific discharge capacity and subsequent reversible capacity but also realize a low charge voltage <3.61 V and a small discharge-charge potential gap of 0.61 V, with the corresponding energy efficiency as high as 83.8%. The combination of ex situ/in situ experimental investigations and theoretical calculations revealed that the 4H/fcc Ir nanostructures are more favorable for the reversible formation of amorphous/low-crystalline discharge products through Ir-O coupling, thereby lowering the overpotential and promoting the cycling stability. This work suggests that preparing catalysts with unconventional phases could be a feasible and promising strategy to boost the performance of next-generation energy conversion and storage systems.

Materials and Methods

Growth of Unconventional 4H/fcc Nanostructures on the Au Template. In general, 4H/fcc Au NRs were used as the template for the growth of 4H/fcc Ir nanostructures. In a typical experiment, 2.5 mL of 4H/fcc Au stock solution was used for the growth of Ir with unconventional phase. Before the overgrowth of Ir, the 4H/fcc Au NRs were carefully dispersed in 1.5 mL of ethanol (solution I). A total of 5 mL of 3 mM $IrCl_3{\cdot}3H_2O$ aqueous solution was mixed with 2.5 mL of 1.2 M KI aqueous solution and then heated at 97 °C for 0.5 h under magnetic stirring (solution II). Solution II at 50 μL was introduced into 1.5 mL of solution I, followed by sonication until the solution became homogenous and transparent. Subsequently, 720 μL of 20 mM $NaBH_4$ in ethanol was rapidly injected into the mixed solution and kept at room temperature for 25 min, without any external disturbance. The Au@4H/fcc-$Ir_{0.14}$ was obtained by centrifugation. Other Au/Ir samples were prepared by the same method but with modified parameters. More preparation details are described in the *SI Appendix*.

Battery Assembly and Electrochemical Measurements. All of the obtained active materials were redispersed in glacial acetic acid and stirred overnight at 40 °C to remove the surface ligands. To prepare cathodes, the obtained catalysts were directly mixed with Nafion ($5\%_{wt}$ in ethanol) at a weight ratio of 9:1 without adding any other carbon species in the mixture of isopropanol and water. The mass loading of total metal was controlled within 0.6 to 0.8 mg per electrode to enable the reliability of electrochemical tests. The electrochemical performance of Li-CO_2 batteries was evaluated using CR2032 coin-type cells, with several holes on the cathode side to allow CO_2 permeation. A piece of commercial Li chip acted as the counter and reference electrodes. The electrolyte was 1 M lithium bis(trifluoromethane sulfonimide) (LiTFSI) and 0.3 M $LiNO_3$ dissolved in DMSO. The assembled Li-CO_2 batteries were tested in a dried and sealed chamber, which was filled with pure CO_2 gas at 80 sccm for at least 15 min to ensure the gas purity inside.

Characterization. X-ray diffraction measurements were conducted on a Bruker D2 and D8 diffractometer using Cu KR radiation at a wavelength of 1.5406 Å. SEM and EDS were acquired by a Thermo Scientific (Waltham, MA) Quattro S scanning electron microscope. A JEOL JEM-2100F (JEOL, Tokyo, Japan) field emission transmission electron microscope was used to collect TEM and high-resolution TEM images. The spherical aberration–corrected HAADF-STEM images and EDS elemental mappings were obtained on a JEOL ARM200F with cold field emission gun and double hexapole Cs correctors (CEOS GmbH, Heidelberg, Germany). Raman spectra were recorded on the LabRAM HR Raman spectrometer with laser excitation at 514.5 nm from an Ar ion laser source. XPS analysis was based on a ESCALAB 220i-XL electron spectrometer from VG Scientific (Waltham, MA) using 300 W Al KR radiation (base pressure $<10^{-5}$ mbar). X-ray absorption spectroscopy was conducted in a transmission mode at beamline X-ray absorption fine structure for catalysis of a Singapore Synchrotron Light Source (Singapore) operated at 700 MeV with a beam current of 200 mA.

Theoretical Calculations. The mainly exposed (004), $(1\bar{1}0)$, and (110) surfaces in 4H Ir nanostructures and 4H Au substrates were established. For comparison, the thermodynamically abundant (111) surfaces of fcc Ir and fcc Au were also considered in the simulations. All of the computational simulations were performed based on DFT calculations with the plane-wave technique, which is implemented in the Vienna ab initio simulation package. Gradient-corrected exchange-correlation functional of Perdew-Burke-Ernzerhof models were used under the projector augmented wave method, with a cutoff kinetic energy of 500 eV for plane-wave basis. The convergence criterion of the total energy was set up to be within 1×10^{-5} eV, while all of the atoms and geometries were optimized until the residual forces became $<1 \times 10^{-2}$ eV/Å. More calculation details are provided in the *SI Appendix*.

Data, Materials, and Software Availability. All of the study data are included in the article and/or supporting information.

ACKNOWLEDGMENTS. This work was supported by grants (project no. 22005258, 22175148, 52102320, 52025025, and 22075291) from the National Natural Science Foundation of China, the Foundation for the Youth S&T Innovation Team of Sichuan Province (project no. 2020JDTD0035), and ITC via the Hong Kong branch of the NPMM, grants (project no. 9610480, 7005512, 7005600, and 9680301) from the City University of Hong Kong, and a Start-Up Grant (project no. 4930977) from The Chinese University of Hong Kong.

Author affiliations: [a]Department of Chemistry, City University of Hong Kong, Kowloon, Hong Kong SAR 999077, China; [b]Hong Kong Branch of National Precious Metals Material Engineering Research Center (NPMM), City University of Hong Kong, Kowloon, Hong Kong SAR 999077, China; [c]Department of Mechanical and Aerospace Engineering, The Hong Kong University of Science and Technology, Clear Water Bay, Hong Kong SAR 999077, China; [d]Institute of Chemical Materials, China Academy of Engineering Physics, Mianyang 621900, Sichuan, China; [e]Institute of Chemical and Engineering Sciences, A*STAR, 1 Pesek Road, Jurong Island, Singapore 627833, Singapore; [f]Institute of Physics, Beijing National Laboratory for Condensed Matter Physics, Chinese Academy of Sciences, Beijing 100190, China; [g]School of Physical Sciences, University of Chinese Academy of Sciences, Beijing 100049, China; [h]Department of Chemistry, Tsinghua University, Beijing 100084, China; [i]Department of Chemistry, The Chinese University of Hong Kong, Shatin, Hong Kong SAR 999077, China; [j]Institute of Fundamental and Frontiers Sciences, University of Electronic Sciences and Technology of China, Chengdu 611731, China; [k]Center of Super-Diamond and Advanced Films (COSDAF), City University of Hong Kong, Kowloon, Hong Kong SAR 999077, China; and [l]City University of Hong Kong Shenzhen Research Institute, Shenzhen 518057, China

Author contributions: Z.F. proposed the research direction and guided the project. J.Z. and Z.F. designed the research. J.Z., T.W., L.C., L.L., Y.W., S.X., B.C., T.L., Q.Z., C.Y., X.Z., Z.G., L.Z., Z.H., G.W., J.W., J.Y., Y.M., P.L., Y.X., S.L., J.C., L.G., T.Z., and Z.F. performed the research. J.Z., T.W., L.C., L.L., Y.C., B.W., C.-S.L., J.C., L.G., T.Z., and Z.F. analyzed and discussed the data and experimental results and drafted the manuscript. J.Z. and L.L. performed the synthesis. J.Z., Y.W., J.Y., and Y.M. carried out the electrochemical experiments. T.W. and T.Z. conducted the DFT calculations. J.Z., L.C., B.W., and J.C. conducted the in situ DEMS tests. S.X. and C.Y. conducted and analyzed the XANES and EXAFS measurements. B.C., T.L., Q.Z., and L.G. performed the aberration-corrected HAADF-STEM characterizations. Z.G. and C.-S.L. conducted the XPS measurements. G.W. and Y.C. implemented the XRD characterizations. J.Z. performed the Raman tests. J.Z., Y.W., X.Z., L.Z., Z.H., J.W., P.L., Y.X., and S.L. performed some supporting experiments. J.Z. and Z.F. wrote the paper.

1. J. Zhou, J. Cheng, B. Wang, H. Peng, J. Lu, Flexible metal-gas batteries: A potential option for next-generation power accessories for wearable electronics. *Energy Environ. Sci.* **13**, 1933–1970 (2020).
2. X. Mu, H. Pan, P. He, H. Zhou, Li-CO_2 and Na-CO_2 batteries: Toward greener and sustainable electrical energy storage. *Adv. Mater.* **32**, 1903790 (2020).
3. D. Aurbach, B. D. McCloskey, L. F. Nazar, P. G. Bruce, Advances in understanding mechanisms underpinning lithium-air batteries. *Nat. Energy* **1**, 16128 (2016).
4. Y. Y. Birdja *et al.*, Advances and challenges in understanding the electrocatalytic conversion of carbon dioxide to fuels. *Nat. Energy* **4**, 732–745 (2019).
5. Z. Xie, X. Zhang, Z. Zhang, Z. Zhou, Metal-CO_2 batteries on the road: CO_2 from contamination gas to energy source. *Adv. Mater.* **29**, 1605891 (2017).
6. B. Chen, X. Zhong, G. Zhou, N. Zhao, H. M. Cheng, Graphene-supported atomically dispersed metals as bifunctional catalysts for next-generation batteries based on conversion reactions. *Adv. Mater.* **34**, 2105812 (2021).
7. B. Liu *et al.*, Recent advances in understanding Li-CO_2 electrochemistry. *Energy Environ. Sci.* **12**, 887–922 (2019).
8. X. Chi *et al.*, A highly stable and flexible zeolite electrolyte solid-state Li-air battery. *Nature* **592**, 551–557 (2021).
9. S. Yang *et al.*, A reversible lithium-CO_2 battery with Ru nanoparticles as a cathode catalyst. *Energy Environ. Sci.* **10**, 972–978 (2017).
10. Y. Liu, R. Wang, Y. Lyu, H. Li, L. Chen, Rechargeable Li/CO_2-O_2 (2:1) battery and Li/CO_2 battery. *Energy Environ. Sci.* **7**, 677 (2014).
11. X. Zhang *et al.*, Rechargeable Li-CO_2 batteries with carbon nanotubes as air cathodes. *Chem. Commun. (Camb.)* **51**, 14636–14639 (2015).
12. X. Li *et al.*, Bamboo-like nitrogen-doped carbon nanotube forests as durable metal-free catalysts for self-powered flexible Li-CO_2 batteries. *Adv. Mater.* **31**, 1903852 (2019).
13. Y. Li *et al.*, Highly surface-wrinkled and N-doped CNTs anchored on metal wire: A novel fiber-shaped cathode toward high-performance flexible Li-CO_2 batteries. *Adv. Funct. Mater.* **29**, 1808117 (2019).
14. Z. Zhang *et al.*, The first introduction of graphene to rechargeable Li-CO_2 batteries. *Angew. Chem. Int. Ed. Engl.* **54**, 6550–6553 (2015).
15. L. Qie, Y. Lin, J. W. Connell, J. Xu, L. Dai, Highly rechargeable lithium-CO_2 batteries with a boron- and nitrogen-codoped holey-graphene cathode. *Angew. Chem. Int. Ed. Engl.* **56**, 6970–6974 (2017).
16. B. Chen *et al.*, Engineering the active sites of graphene catalyst: From CO_2 activation to activate Li-CO_2 batteries. *ACS Nano* **15**, 9841–9850 (2021).
17. Y. Jin *et al.*, High-performance Li-CO_2 batteries based on metal-free carbon quantum dot/holey graphene composite catalysts. *Adv. Funct. Mater.* **28**, 1804630 (2018).
18. C. Hu *et al.*, Carbon-based metal-free catalysts for energy storage and environmental remediation. *Adv. Mater.* **31**, 1806128 (2019).
19. K. Baek *et al.*, Synergistic effect of quinary molten salts and ruthenium catalyst for high-power-density lithium-carbon dioxide cell. *Nat. Commun.* **11**, 456 (2020).
20. Y. Qiao *et al.*, Li-CO_2 electrochemistry: A new strategy for CO_2 fixation and energy storage. *Joule* **1**, 359–370 (2017).
21. Y. Qiao *et al.*, Synergistic effect of bifunctional catalytic sites and defect engineering for high-performance Li-CO_2 batteries. *Energy Storage Mater.* **27**, 133–139 (2020).
22. Y. Xing *et al.*, Crumpled Ir nanosheets fully covered on porous carbon nanofibers for long-life rechargeable lithium-CO_2 batteries. *Adv. Mater.* **30**, 1803124 (2018).
23. C. Wang *et al.*, Fabricating Ir/C nanofiber networks as free-standing air cathodes for rechargeable Li-CO_2 batteries. *Small* **14**, 1800641 (2018).
24. Z. Zhang *et al.*, Verifying the rechargeability of Li-CO_2 batteries on working cathodes of Ni nanoparticles highly dispersed on N-doped graphene. *Adv. Sci. (Weinh.)* **5**, 1700567 (2017).
25. H.-S. Kim, J.-Y. Lee, J.-K. Yoo, W.-H. Ryu, Capillary-driven formation of iron nanoparticles embedded in nanotubes for catalyzed lithium–carbon dioxide reaction. *ACS Mater. Lett.* **3**, 815–825 (2021).
26. C. Hu *et al.*, High-performance, long-life, rechargeable Li-CO_2 batteries based on a 3D holey graphene cathode implanted with single iron atoms. *Adv. Mater.* **32**, 1907436 (2020).
27. B. W. Zhang *et al.*, Targeted synergy between adjacent Co atoms on graphene oxide as an efficient new electrocatalyst for Li–CO_2 batteries. *Adv. Funct. Mater.* **29**, 1904206 (2019).
28. Z. Zhang *et al.*, Exploiting synergistic effect by integrating ruthenium-copper nanoparticles highly co-dispersed on graphene as efficient air cathodes for Li-CO_2 batteries. *Adv. Energy Mater.* **9**, 1802805 (2019).
29. Z. Zhang *et al.*, Identification of cathode stability in Li-CO_2 batteries with Cu nanoparticles highly dispersed on N-doped graphene. *J. Mater. Chem. A Mater. Energy Sustain.* **6**, 3218–3223 (2018).
30. Y. Jin, F. Chen, J. Wang, Achieving low charge overpotential in a Li-CO_2 battery with bimetallic RuCo nanoalloy decorated carbon nanofiber cathodes. *ACS Sustain. Chem. Eng.* **8**, 2783–2792 (2020).
31. Y. Xing *et al.*, Ultrathin RuRh alloy nanosheets enable high-performance lithium-CO_2 battery. *Matter* **2**, 1494–1508 (2020).
32. Y. Hou *et al.*, Mo_2C/CNT: An efficient catalyst for rechargeable Li-CO_2 batteries. *Adv. Funct. Mater.* **27**, 1700564 (2017).
33. J. Zhou *et al.*, A quasi-solid-state flexible fiber-shaped Li-CO_2 battery with low overpotential and high energy efficiency. *Adv. Mater.* **31**, 1804439 (2019).
34. R. Pipes, J. He, A. Bhargav, A. Manthiram, Freestanding vanadium nitride nanowire membrane as an efficient, carbon-free gas diffusion cathode for Li-CO_2 batteries. *Energy Storage Mater.* **31**, 95–104 (2020).
35. G. Wu *et al.*, Design of ultralong-life Li-CO_2 batteries with IrO_2 nanoparticles highly dispersed on nitrogen-doped carbon nanotubes. *J. Mater. Chem. A Mater. Energy Sustain.* **8**, 3763–3770 (2020).
36. Z. Guo *et al.*, A highly reversible long-life Li-CO_2 battery with a RuP_2-based catalytic cathode. *Small* **15**, 1803246 (2019).
37. H. Wang *et al.*, Realizing interfacial electronic interaction within ZnS quantum dots/N-rGO heterostructures for efficient Li–CO_2 batteries. *Adv. Energy Mater.* **9**, 1901806 (2019).
38. S. Li *et al.*, Monodispersed MnO nanoparticles in graphene-an interconnected N-doped 3D carbon framework as a highly efficient gas cathode in Li–CO_2 batteries. *Energy Environ. Sci.* **12**, 1046–1054 (2019).
39. Z. Zhang, W.-L. Bai, K.-X. Wang, J.-S. Chen, Electrocatalyst design for aprotic Li-CO_2 batteries. *Energy Environ. Sci.* **13**, 4717–4737 (2020).
40. Y. Chen *et al.*, Phase engineering of nanomaterials. *Nat. Rev. Chem.* **4**, 243–256 (2020).
41. Z. Fan, H. Zhang, Template synthesis of noble metal nanocrystals with unusual crystal structures and their catalytic applications. *Acc. Chem. Res.* **49**, 2841–2850 (2016).
42. S. Lu *et al.*, Crystal phase control of gold nanomaterials by wet-chemical synthesis. *Acc. Chem. Res.* **53**, 2106–2118 (2020).
43. Z. Fan, X. Huang, Y. Chen, W. Huang, H. Zhang, Facile synthesis of gold nanomaterials with unusual crystal structures. *Nat. Protoc.* **12**, 2367–2378 (2017).
44. Z. Fan, H. Zhang, Crystal phase-controlled synthesis, properties and applications of noble metal nanomaterials. *Chem. Soc. Rev.* **45**, 63–82 (2016).
45. Z. Fan *et al.*, Epitaxial growth of unusual 4H hexagonal Ir, Rh, Os, Ru and Cu nanostructures on 4H Au nanoribbons. *Chem. Sci. (Camb.)* **8**, 795–799 (2017).
46. Z. Fan *et al.*, Heterophase fcc-2H-fcc gold nanorods. *Nat. Commun.* **11**, 3293 (2020).
47. Y. Wang *et al.*, Undercoordinated active sites on 4H gold nanostructures for CO_2 reduction. *Nano Lett.* **20**, 8074–8080 (2020).
48. Y. Ge *et al.*, Phase-selective epitaxial growth of heterophase nanostructures on unconventional 2H-Pd nanoparticles. *J. Am. Chem. Soc.* **142**, 18971–18980 (2020).
49. Z. Fan *et al.*, Stabilization of 4H hexagonal phase in gold nanoribbons. *Nat. Commun.* **6**, 7684 (2015).
50. Y. Chen *et al.*, Ethylene selectivity in electrocatalytic CO_2 reduction on Cu nanomaterials: A crystal phase-dependent study. *J. Am. Chem. Soc.* **142**, 12760–12766 (2020).
51. M. Park *et al.*, Regulating the catalytic dynamics through a crystal structure modulation of bimetallic catalyst. *Adv. Energy Mater.* **10**, 1903225 (2020).
52. H. Wang *et al.*, Significantly enhanced overall water splitting performance by partial oxidation of Ir through Au modification in core-shell alloy structure. *J. Am. Chem. Soc.* **143**, 4639–4645 (2021).
53. Z. Zhao, Y. Su, Z. Peng, Probing lithium carbonate formation in trace-O_2-assisted aprotic Li-CO_2 batteries using in situ surface-enhanced Raman spectroscopy. *J. Phys. Chem. Lett.* **10**, 322–328 (2019).
54. L. Johnson *et al.*, The role of LiO_2 solubility in O_2 reduction in aprotic solvents and its consequences for Li-O_2 batteries. *Nat. Chem.* **6**, 1091–1099 (2014).
55. X. Gao, Y. Chen, L. Johnson, P. G. Bruce, Promoting solution phase discharge in Li-O_2 batteries containing weakly solvating electrolyte solutions. *Nat. Mater.* **15**, 882–888 (2016).
56. A. Khurram, Y. Yin, L. Yan, L. Zhao, B. M. Gallant, Governing role of solvent on discharge activity in lithium-CO_2 batteries. *J. Phys. Chem. Lett.* **10**, 6679–6687 (2019).
57. Y. Chen, S. A. Freunberger, Z. Peng, O. Fontaine, P. G. Bruce, Charging a Li-O_2 battery using a redox mediator. *Nat. Chem.* **5**, 489–494 (2013).
58. Z. Peng, S. A. Freunberger, Y. Chen, P. G. Bruce, A reversible and higher-rate Li-O_2 battery. *Science* **337**, 563–566 (2012).

59. Y. Kong *et al.*, Nano-sized Au particle-modified carbon nanotubes as an effective and stable cathode for Li-CO_2 batteries. *Eur. J. Inorg. Chem.* **2021**, 590–596 (2021).
60. Z. Fan *et al.*, Synthesis of 4H/fcc-Au@M (M = Ir, Os, IrOs) core-shell nanoribbons for electrocatalytic oxygen evolution reaction. *Small* **12**, 3908–3913 (2016).
61. Y. Zhang *et al.*, Amorphous Li_2O_2: Chemical synthesis and electrochemical properties. *Angew. Chem. Int. Ed.* **128**, 10875–10879 (2016).
62. M. A. Tamor, W. C. Vassell, Raman "fingerprinting" of amorphous carbon films. *J. Appl. Phys.* **76**, 3823–3830 (1994).
63. J. Wagner, M. Ramsteiner, C. Wild, P. Koidl, Resonant Raman scattering of amorphous carbon and polycrystalline diamond films. *Phys. Rev. B Condens. Matter* **40**, 1817–1824 (1989).
64. Y. Zhu *et al.*, Tandem catalysis in electrochemical CO_2 reduction reaction. *Nano Res.* **14**, 4471–4486 (2021).
65. A. Khurram, M. He, B. M. Gallant, Tailoring the discharge reaction in Li-CO_2 batteries through incorporation of CO_2 capture chemistry. *Joule* **2**, 1–18 (2018).
66. Y. Wang, J. Lv, L. Zhu, Y. Ma, CALYPSO: A method for crystal structure prediction. *Comput. Phys. Commun.* **183**, 2063–2070 (2012).